Astron. Astrophys. 325, 57–73 (1997)

ASTRONOMY
AND
ASTROPHYSICS

The synchrotron spectra of radio hot spots

II. Infrared imaging

K. Meisenheimer, M.G. Yates, and H.-J. Röser

Max-Planck-Institut für Astronomie, Königstuhl 17, D-69117 Heidelberg

Received 5 August 1996 / Accepted 31 January 1997

Abstract. We present infrared imaging of a sample of 11 hot spots in the lobes of powerful radio galaxies. We have detected infrared counterparts to the hot spots in 3C 20 West, 3C 33 South, 3C 111 East and 3C 303 West all of which have known optical counterparts as well. In addition, we detected the radio jet of 3C 303 in the near infrared. Four other hot spots, those in 3C 20 East, 3C 65 (both sides), and 3C 123 East were not detected in the infrared. The optical candidates for the hot spots A and B in the western lobe of Cygnus A (3C 405) were visible in the infrared but their optical-infrared spectra reveal them both to be galactic stars. Neither infrared nor optical candidate was found for hot spot D in the eastern lobe of Cygnus A. We use the detections together with flux measurements at other frequencies to construct synchrotron spectra of the hot spots from the radio to the optical. Adding the bright hot spots in Cygnus A, the synchrotron spectra of which are well constrained by our upper limits and the millimetre flux, we are able to extend our general analysis of synchrotron spectra to 8 hot spots. We confirm our previous claim that first order Fermi acceleration could account for the particle acceleration in most hot spots but also provide evidence for our suspicion that the full range of physical parameters is much broader then our original sample indicated. However, in some well extended hot spots an additional acceleration process seems to be required.

Key words: radiation mechanism: non-thermal – radio continuum: galaxies – galaxies: general

1. Introduction

This paper presents infrared imaging observations of a sample of hot spots in the lobes of powerful, low-redshift, classical double radio sources, and is thus an extension of our multi-wavelength imaging and polarimetry observations of hot spots in radio sources (Meisenheimer et al. 1989, hereafter Paper I). Hot spots are frequently found near the outermost edges of the lobes of powerful, classical FRII radio sources, and are characterised by their high radio surface brightness. In a seminal paper, Blandford & Rees (1974) explained these hot spots as the "working surfaces" of supersonic jets in which the jet's kinetic energy is partly dissipated into the acceleration of relativistic particles, giving rise to the observed intense synchrotron radiation. Their hypothesis was later impressively confirmed by several cases in which narrow radio jets connecting the core of the radio source with the hot spot have been observed (e.g. Cygnus A, 3C 111, Pictor A).

The first conclusive evidence that the synchrotron spectra of these hot spots extend up to optical frequencies was provided by Meisenheimer & Röser (1986) who showed that the optical counterpart to the radio hot spot 3C 33 South is strongly polarized (29%). Subsequent work has concentrated on the acquisition of data for further hot spots over as large a wavelength range as possible and the first results of this multi-wavelength campaign were presented in Paper I. This multi-wavelength approach is motivated by the need to obtain an accurate measure of the shape of the spectrum so as to constrain the nature of the acceleration mechanism which is able to produce electrons at ultra-relativistic energies emitting the observed synchrotron light. Paper I showed that the infrared data are of great importance in determining the shape accurately, especially given the wide gap between the radio and optical parts of the spectra and presented firm K-band detections of two hot spots (3C 33 S and 3C 111 E) and an upper limit for 3C 123 E (all obtained with aperture photometry). This work presents new infrared imaging for these three hot spots in order to improve on their photometry as well as infrared imaging for a further eight examples.

Specifically, Paper I showed for the first time that the hot spot spectra could be accurately modelled by first-order Fermi acceleration at a strong shock. Our original aim has been to construct spectra for a larger number of hot spot candidates and to confirm the first order Fermi acceleration interpretation. However, in the last years there have been various observational indications that particle acceleration in extended radio sources is not confined to the hot spots or bright knots but might be distributed throughout a large fraction of the entire radio source

Send offprint requests to: K. Meisenheimer

(Neumann et al. 1995, Perley et al. 1997). Thus the hot spot spectra have to be discussed in this wider context.

Section 2 presents details of the observations, and Section 3 gathers together the available multi-wavelength data for each hot spot and presents their spectra. The new results are related to previous studies in Section 4 in order to derive general properties of the underlying particle acceleration mechanism.

2. Observations

2.1. Object selection

The sample of 11 hot spot candidates observed in the present work (and listed in Table 1) includes most of the radio-bright sources accessible from the northern hemisphere for which deep optical imaging and high-resolution radio maps have already been obtained either by ourselves or other authors. Optical polarization data, and millimetre wavelength data also exist for some of the sources. It does not however constitute a statistically complete sample.

The hot spots in 3C 33 S and 3C 111 E were both observed and detected in the infrared at UKIRT in 1986 with a single aperture photometer (as described in Paper I) but it was important to check these results with imaging, given that in both cases bright contaminating stars lie only five arcsec from the optical counterpart to the hot spot. Those earlier data were obtained with a five arcsec aperture (the smallest aperture that one may practically use with the photometer at UKIRT) and it was necessary to model and subtract the flux from the contaminating stars in each case in order to derive an accurate measure of the infrared hot spot flux. The hot spot in 3C 20 W was observed by Hiltner et al. (1994) to be polarized in the optical but was not observed in the infrared in 1986 and so was a prime candidate for imaging in the infrared. A one-dimensional K-band scan of the hot spot in 3C123E was obtained with the aperture photometer at UKIRT in 1986 resulting in a tentative detection (Paper I) and it was thus of great interest to improve on this result with imaging. Given the largely improved limiting brightness attainable with infrared imaging and the steepness of most hot spot spectra in the infrared-optical regime makes searching for infrared counterparts a reasonable proposition, even in the absence of an optical candidate. For instance, there is a hot spot in the eastern lobe of 3C 20 without an optical candidate and this was observed in the infrared along with that in the western lobe. In addition, infrared detections can provide a strong constraint on the location of any cut-offs in the spectra, even if the faintness of an optical counterpart prohibits the determination of a good optical spectral index. Thus, the remaining candidates were chosen mainly on the grounds of high radio surface brightness, the availability of good radio mapping, and supplemented in most cases by the availability of deep optical imaging which suggested the presence of a possible optical counterpart to the hot spot. The radio hot spots of Cygnus A (3C 405) have been the subject of extensive imaging and polarimetry campaigns by the present authors. Despite the proximity and high radio power of this radio galaxy, attempts to locate optical candidates for the hot spots have been difficult. In the western lobe, our imaging (and that of earlier workers) suggests possible optical counterparts to hot spots A & B (in the nomenclature of Hargrave & Ryle 1974), but in the eastern lobe (hot spot D in the same nomenclature) no optical counterpart has so far been located. The hot spot in the western lobe of the well studied source 3C 303 has a diffuse optical counterpart (Kronberg 1976), although this identification has not been confirmed by a polarization measurement yet. 3C 65 is an extremely distant radio source (z = 1.176) but it has two hot spots which are very bright in the radio, and this makes an attempt at finding an infrared counterpart worthwhile.

2.2. Infrared imaging

The hot spots listed in Table 1 were imaged with IRCAM in the K-band at the United Kingdom Infrared Telescope (UKIRT) during two observing runs in 1989. IRCAM employed an SBRC Indium-Antimonide detector with 58x62 pixels, and for these observations a pixel scale of 0.62 arcsec per pixel was used (resulting in a field of view of about 30 arcsec on a side). Each hot spot field was imaged by obtaining a number of successive integrations of 300s duration, and offsetting the telescope by a few arcsecs in a random direction after each 300s exposure so as to aid in the construction of a flat field using a superposition of the science frames. Most of our fields were uncrowded enough to make this technique feasible, and it eliminates the necessity for separate sky exposures. It also provides much better sky subtraction than individual sky frames, possibly separated from the data frames themselves by a time interval that is much greater than the typical timescale over which significant variations in the infrared sky occur.

Table 1 shows the total integration times obtained for the observed hot spots. It is worth noting in connection with the choice of on-chip integration time used here that subsequent experience by other observers using this and other infrared cameras of similar type (e.g. Cowie et al. 1990) indicates that the optimal integration time for each individual exposure (in order to provide the best estimate of the sky background) should be a little longer than the time needed to reach the sky-limited regime, that is about 80s in the K-band for this particular camera and telescope. Despite the longer than optimum on-chip exposure time employed in the current work, our reduced images are generally flatter than one part in 10^4 when measured on a pixel-to-pixel basis.

All of the data were obtained during photometric conditions, apart from the latter half of the night of 1989 June 10 which affected the image of the two hot spots in the western lobe of 3C405 (hot spots A and B). This non-photometric image was subsequently calibrated with a 560s calibration frame obtained during photometric weather at UKIRT on 1991 July 10 (and provided to us courtesy of the Service Observations scheme). This calibration frame was obtained with exactly the same instrumentation as our deeper imaging carried out in 1989, and was constructed in the same manner (i.e. from a series of shifted, short-exposure frames). All of our data were taken at airmasses less than 1.3, and standard stars were observed every night.

Table 1. Hot spots observed (coordinates refer to the peak of the radio emission).

Hotspot	z	RA (1950.0)	Dec. (1950.0)	Date observed [U.T.]	Int. time [sec]	Notes
3C 20 West	0.174	00 40 17.4	+51 47 16	1989 Nov. 25	1800	(1)
3C 20 East	0.174	00 40 22.4	+51 47 06	1989 Nov. 24	1800	(2)
3C 33 South	0.060	01 06 12.1	+13 02 27	1989 Nov. 24	1800	
3C 65 E+W	1.176	02 20 36.3	+39 47 18	1989 Nov. 24	1800	(3)
3C 111 East	0.049	04 15 09.7	+37 55 15	1989 Nov. 24	1500	
3C 123 East	0.218	04 33 55.8	+29 34 10	1989 Nov. 25	1800	
3C 303 West	0.141	14 41 23.1	+52 14 21	1989 Jun. 10	4500	(4)
3C 405A+B	0.057	19 57 39.0	+40 36 10	1989 Jun. 10	2700	(5), (7)
3C 405D	0.057	19 57 49.1	+40 35 34	1989 Jun. 10	3600	(6)

Notes:
(1) Coordinates of the brighter of the two components in the western lobe are given. This is hot spot B in the 15 GHz map of Paper I.
(2) The eastern hot spot consists of two components, A and B in the notation of Laing (1981). Coordinates for the compacter component A are given.
(3) Both hot spots were imaged simultaneously in a single frame.
(4) Coordinates of the southern hot spot in the western lobe are given. This is A_1 in the notation of Lonsdale et al. (1983).
(5) The western lobe contains two distinct hot spots, A and B in the notation of Hargrave & Ryle (1974): they were observed simultaneously in the same image.
(6) The single hot spot in the eastern lobe is labelled D in the notation of Hargrave & Ryle (1974).
(7) These data were obtained in non-photometric conditions. A 560s calibration frame was obtained on 1991 Jul. 10. See text for details.

2.3. Data reduction

The dark current and bias level was subtracted from each of the individual exposures using suitably scaled dark frames obtained each night (a standard non-linearity correction had already been made to the data). Permanently bad pixels were then corrected by interpolation using a map of the known bad-pixel positions. Sky frames were constructed for each source using the individual 300s exposures (and using only the data for that source rather than data obtained earlier or later in the night). The median of the pixel values at each given pixel position was calculated and a median sky frame constructed from these values. In a second step, each individual frame is compared with this median and all pixels more discrepant than a certain threshold (i.e. the pixel illuminated by objects) are flagged. A new median is calculated by ignoring the flagged pixels. This process is iterated if necessary. Finally the un-flagged pixel values are *averaged* to obtain the optimum *blank sky frame.* The data frames were then flattened by division of a normalised version of this sky frame. Any remaining bad or hot pixels were then dealt with before stacking the individual frames. The data for each source were stacked after a rebinning process which simultaneously accounts for the different registration and variation of the seeing point-spread-function (PSF) of the individual frames. Offsets and PSF have been determined from bright stars in each field.

Fig. 1 shows grey scales of the hot spots imaged. The field of view which received the full integration time (and is shown here) is smaller than the nominal field provided by the chip because of the shifting of the individual exposures. The hot spot identifications and detections are discussed in Section 3 below.

2.4. Photometry

Table 2 presents infrared photometry of the detected hot spot candidates and limiting magnitudes in the cases where no detection was made. The calibration was done with respect to standard stars observed in the same night and should be accurate to better than 10%. We give the photometric results both un-corrected and corrected for galactic extinction. Galactic extinction estimates (A_K) were taken either from Paper I or from the HI maps of Burstein & Heiles (1982) with the assumption that A_K/A_V = 0.112 (Rieke & Lebofsky 1985). 3C405 (Cygnus A) lies at low Galactic latitude and the reddening is not accurately known. We have derived a mean value for A_V from the $E(B-V)$ estimates of van den Bergh (1976), Yee & Oke (1978) and Spinrad & Stauffer (1982), which are 0.39, 0.50 and 0.36 respectively. For the absolute flux calibration we assume a Vega flux S_K = 657 Jy (as in Paper I). Our photometry generally refers to a 5 arcsec diameter aperture, except in cases where there are close contaminating objects in which case a smaller aperture is used. In the case of 3C 303 west the infrared emission appears to be extended: the value shown in Table 2 was obtained using a 4 arcsec diameter aperture centered on the brightest part of the optical emission. The optical and infrared candidate for hot spot A of 3C 405 is another problematic object in that it is merged with a nearby star. Rather than attempt to model (probably erroneously) the star's contribution to the in-

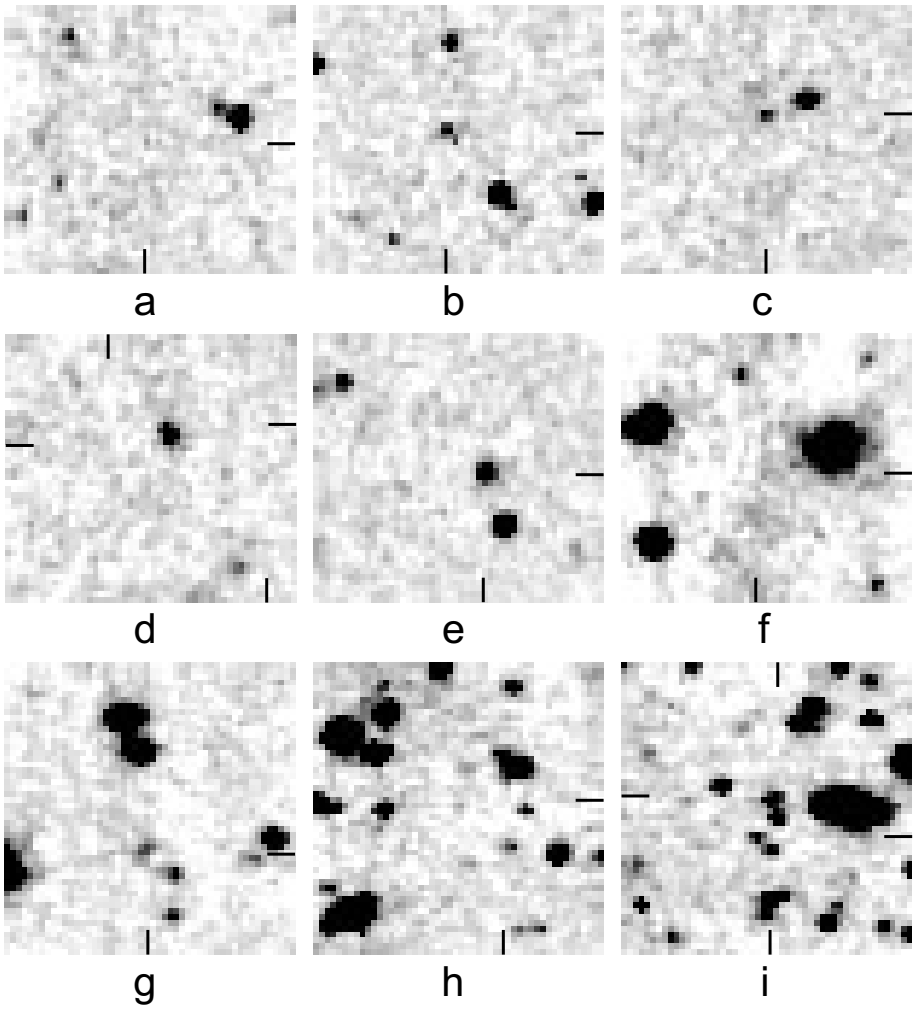

Fig. 1a–i. Grey scales of the K-band images of hot spots. Each pixel subtends 0.62 arcsec. North is at the top of each image and east to the left. The dynamic range is adjusted to $-3\sigma_b, +6\sigma_b$ around the background level. Black tick marks at the lower and right boundary of each image indicate the hot spot positions. In those fields in which two radio hot spots are present a second pair of tick marks (left and upper) is given. **a** 3C 20 East; **b** 3C 20 West; **c** 3C 33 South; **d** 3C 65, both lobes; **e** 3C 111 East; **f** 3C 123 East; **g** 3C 303 West; **h** 3C405 East: hot spot D; **i** 3C 405 West: hot spots A and B.

Table 2. K-band photometry of hotspots.

Hotspot	S_ν(obs.)		S_ν(corr.)		Aper.	A_K	Notes
	[μJy]	[mag]	[μJy]	[mag]	[arcsec]	[mag]	
3C 20 W	43 ± 2	17.95 ± 0.06	50 ± 2	17.84 ± 0.06	5	0.12	
3C 20 E	< 14	> 19.2	< 16	> 19.06	2	0.12	(1)
3C 33 S	43 ± 5	17.95 ± 0.12	44 ± 5	17.94 ± 0.12	5	0.01	
3C 65 E+W	< 8	> 19.7	< 8	> 19.74	2	0.02	(1)
3C 111 E	87 ± 4	17.20 ± 0.05	105 ± 4	16.99 ± 0.05	5	0.21	
3C 123 E	< 42	> 17.98	< 48	> 17.84	2	0.14	(1)
3C 303 W	43 ± 2	17.9 ± 0.06	43 ± 2	17.95 ± 0.06	4	0.00	(2)
3C 405 A	26	18.49	30	18.35	1.75	0.14	(3)
3C 405 B	31 ± 2	18.31 ± 0.08	35 ± 2	18.17 ± 0.08	2.5	0.14	(3)
3C 405 D	< 22	> 18.7	< 25	> 18.53	2	0.14	(1)

Notes:
(1) Upper limits refer to 5× the background noise measured in a circular aperture of 2″ diameter.
(2) Centre of emission only – see text for details.
(3) Magnitude of star coincident with the hot spot position.

Table 3. Optical photometry of hot spots not contained in Paper I.

Hotspot	λ [nm]	ν [10^{14}]	S_ν(corr.) [μJy]	Ref.	A_V
3C 20 E	648	4.63	< 0.65	[1]	1.09 ± 0.03
3C 65	820	3.66	< 2.0	[2]	0.16 ± 0.03
3C 303W	360	8.33	5.0 ± 1.3	[3]	0.00
	390	7.69	5.5 ± 0.5	[4]	
	430	6.98	5.5 ± 1.1	[3]	
	480	6.25	6.6 ± 0.7	[4]	
	540	5.56	7.5 ± 1.2	[3]	
	790	3.80	9.1 ± 1.0	[4]	
3C 405A	452	6.64	50	[5]	1.26 ± 0.20
	648	4.63	80	[5]	
	863	3.48	100	[5]	
3C 405B	452	6.64	21.9 ± 0.8	[5]	1.26 ± 0.20
	648	4.63	46.2 ± 0.3	[5]	
	863	3.48	52.4 ± 2.6	[5]	
3C 405D	452	6.64	< 5	[5]	1.26 ± 0.20

Note: All fluxes are corrected for Galactic extinction.
References: [1] Hiltner et al. (1994). [2] Estimate from image by Gunn et al. (1981). [3] Lelièvre & Wlérick (1975). [4] Keel (1988). [5] This paper.

Table 4. Radio data for the hotspots not contained in Paper I.

Hotspot	ν [GHz]	S_ν [mJy]	Reference
3C 20 E	4.9	137 ± 5	[1]
	15.0	61 ± 2	[1]
3C 65 W	4.9	276 ± 20	[2]
3C 123 E	98.	517 ± 78	[10]
3C 303 W	0.408	2200 ± 200	[3]
	2.7	450 ± 50[1]	[4]
	5.0	260 ± 30	[5]
3C 405 A	0.151	radio data	
	...	are taken	
	375.	from ref. [6]	
3C 405 B	2.67	24000 ± 2500	[7]
	4.95	11100 ± 200	[7]
	5.0	8000 ± 400	[8]
	15.4	2800 ± 300	[7]
	22.5	1100 ± 50	[9]
	31.	300 ± 100	[7]
3C 405 D	0.151	radio data	
	...	are taken	
	375.	from ref. [6]	

References: [1] Hiltner et al. (1994), [2] own VLA data, [3] Lonsdale et al. (1983), [4] Laing (1981), [5] Pooley & Henbest (1974), [6] Carilli et al. (1991), [7] Alexander et al. (1984), [8] Hargrave & Ryle (1974), [9] Dreher (1981), [10] Okayasu et al. (1992)..

frared hot spot flux (e.g. by modelling the star with a Gaussian) we show instead in Table 2 the infrared flux obtained with a 1.75 arcsec diameter aperture centred on the hot spot's radio position. Since we pursued the same procedure on the optical images in order to get the flux values given in Table 3, the NIR-optical spectrum should be correct while the error of the absolute flux may easily exceed 20%.

Errors are calculated from the error associated with the estimate of the background noise. Limiting fluxes are 5σ detection limits evaluated for a 2 arcsec aperture. The wide variation in limiting magnitudes is largely a result of the variable success in deriving a good sky-flat for each source. For example, the median sky technique used here was less successful for the source 3C123E where a large fraction of all frames is covered by the radio galaxy, thus a brighter limiting magnitude was obtained.

3. The synchrotron spectra of individual sources

In this section we will discuss our new infrared data in connection with the existing multi-wavelength data, as well as with new data we have collected as part of our ongoing multi-wavelength hot spot project. The optical data in Table 3 are those not contained in Paper I and include some unpublished measurements of Cygnus A. Table 4 contains radio data for those hot spots which are not contained in Paper I. The radio flux for Cygnus A, hot spots A and D is taken directly from Table 3 in Carilli et al. (1991) and therefore not repeated in Table 4.

In all cases where we detected an NIR counterpart of the radio hot spot (all of which also have optical detections) we fit synchrotron model spectra to the overall flux distribution. As in Paper I, the synchrotron spectra are modelled by assuming a magnetic field which is randomly distributed in a plane ("Mach disk") inclined by 45° with respect to the plane of sky (*cf.* Table 6). Two different models of the energy distribution of relativistic electrons are taken:

(i) uses the energy spectrum predicted by diffusive shock acceleration including the effect of synchrotron losses as derived by Heavens & Meisenheimer (1987).
(ii) refers to a broken power-law spectrum with instantaneous maximum energy cutoff. This is an idealized form of model (i) which results in the steepest possible cutoff at high frequencies.

Both models are characterized by 4 free parameters: the low frequency spectral index α_0, the cutoff frequency ν_c, the ratio γ_c/γ_b between the cutoff and break energies in the electron spectrum, and a flux normalization S_ν(5 GHz).

These model fits are displayed in Figs. 2. The fit parameters for each source are summarized in Table 5 and histograms in Fig. 4 show their distribution Although no infrared counterparts have been identified useful model fits could also be obtained for 3C 123 and Cygnus A where the millimetre data and K-band upper limits confine the spectra. The following notes on each individual source discuss the spectra and contains further explanatory details where appropriate.

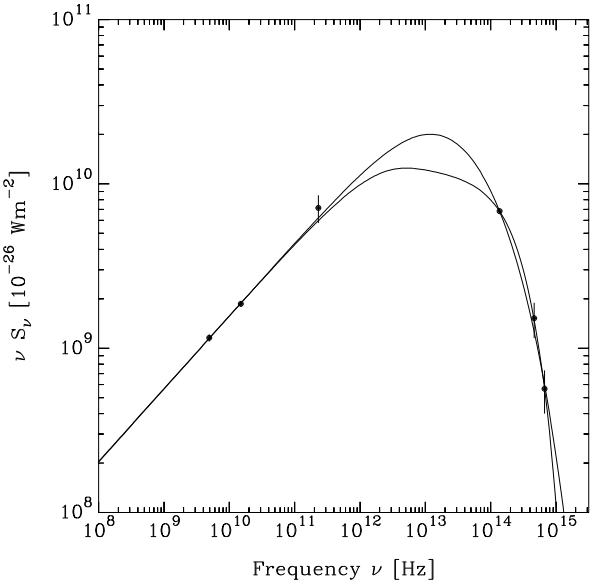

Fig. 2a. Synchroton spectrum of hot spot component B 3C 20 West. The thick line shows the spectral fit assuming model (i). The thin line represents model (ii).

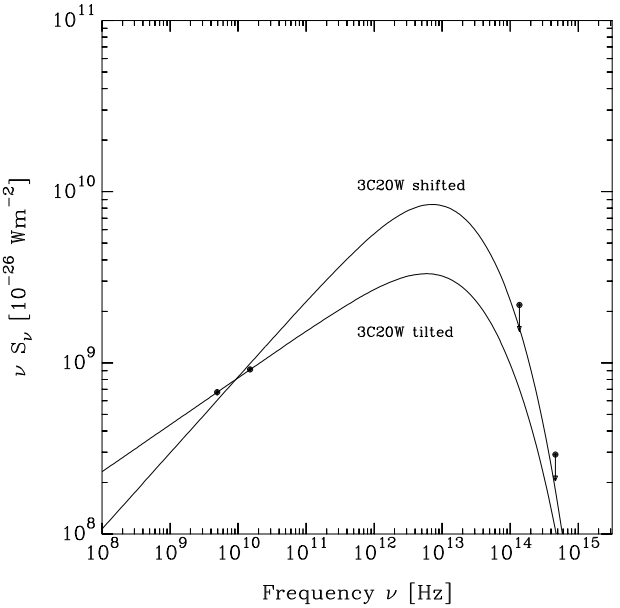

Fig. 2b. Possible spectra of 3C 20 East. The thick line corresponds to the spectrum of 3C 20 W, which was shifted by -0.2 in $\log\nu$. The thin line shows that also a steeper radio-to-optical power-law (with an unchanged cutoff frequency: "3C 20W tilted") could explain the non-detection in the near infrared and optical bands.

3C 20 West. The hot spots in the two lobes of 3C 20 are discussed in detail by Hiltner et al. (1994) and we will take much of the data directly from that work. The western is the stronger of the two hot spots associated with 3C 20. It was already discussed in Paper I. It consists of two components, a southern compact feature (B in the 15 GHz map of Paper I) which has a tail which leads northwards and ends in a secondary intensity peak (component A). Data obtained with a $0\farcs14$ beam resolve B into an elliptical object with dimensions $0\farcs21 \times 0\farcs13$. B has an optical counterpart (photometry is taken from Paper I) and its optical emission is highly polarized (49±7%, Hiltner et al. 1994). The source has also been detected at 1.3 mm with the IRAM telescope (Paper I). The source is clearly detected in our K-band image (Fig. 1a), providing an important new constraint on the overall spectrum. The new spectral fits confirm the parameter values given in Paper I (see Fig. 2a and Table 5). The optical photometry of this faint hot spot is not accurate enough to decide between the model fits (i) and (ii).

3C 20 East. The hot spot complex in the eastern lobe of this radio galaxy is the weaker of the radio lobes, and also consists of two components. Component A is the more compact of the two components ($0\farcs22 \times 0\farcs17$ as measured from data obtained using a $0\farcs14$ beam) and so is best regarded as the primary hot spot. Component B is brighter than A but is more extended, and is edge-brightened. No optical identification was found on a 1500s R-band image obtained at Calar Alto in October 1985 (Hiltner et al. 1994), and the resulting 5σ upper-limit is shown in Table 3. Similarly, no infrared identification has been obtained here (Fig. 1b), providing only the upper limit shown in Table 2. We have no millimetre data for this source as yet. Thus the synchrotron spectrum beyond the radio regime remains undetermined. Nevertheless it can be seen on Fig. 2b that a minor shift in the cutoff spectrum of 3C 20 west would be sufficient to account for the non-detection of 3C 20 east. An alternative possibility would be a steeper radio-to-optical spectrum with the same cutoff frequency as found in 3C 20 W.

3C 33 South. The optical counterpart to this hot spot was the first example observed to be highly polarized ($29.2 \pm 2.4\%$, Meisenheimer & Röser 1986) and was detected in the infrared with the aperture photometer at UKIRT (Paper I). Our infrared image of the hot spot (Fig. 1c) clearly shows an extension to the northeast which is also seen in the optical image. We measure a (corrected) K-band flux for the hot spot of $S_K = (44 \pm 5)$ μJy. Crane & Stockton (1989) present a K-band image of 3C 33 S obtained with exactly the same instrumentation (IRCAM in the 0.62 arcsec per pixel mode) as our own data, and obtain a flux of (49 ± 7) μJy which agrees with our value to within the errors. Although their image involved a total integration time of 6480s (as opposed to our integration time of only 1800s) the sky appears to be noisier than on our own data, probably due to flat-fielding difficulties.

Our earlier flux measurement based on aperture photometry (Paper I, $S_K = (55 \pm 5)$ μJy) is slightly larger than these two measurements on images. Since it was necessary to subtract the contribution from the bright star which lies less than 5 arcsec away in order to derive the flux for the hot spot from that data (by image reconstruction) we consider this small difference as

Table 5. Parameters from the synchrotron model fits.

Hotspot	Model	Spectral index α_0	Cutoff frequency ν_c [10^{14} Hz]	Energy ratio γ_c/γ_b	S_ν(5 GHz) [mJy]	$\chi^2/N_{\rm free}$	Data points
3C 20 west (B)	(i)	-0.56 ± 0.03	1.16 ± 0.04	10 ± 3	231 ± 6	0.55	6
	(ii)	-0.56 ± 0.03	1.83 ± 0.08	9.5 ± 1.2	231 ± 6	0.40	6
3C 33 south	(i)	-0.750 ± 0.010	2.99 ± 0.09	4.4 ± 0.8	611 ± 13	0.90	10
	(ii)	-0.745 ± 0.007	3.06 ± 0.08	10 ± 3	609 ± 13	2.3	10
3C 111 east	(i)	-0.520 ± 0.013	0.46 ± 0.11	< 2	267 ± 6	1.28	8
	(ii)	-0.527 ± 0.010	1.27 ± 0.03	4.5 ± 0.5	269 ± 6	0.90	8
3C 123 east	(i)	-0.45 ± 0.07	0.0060 ± 0.0040	6 ± 1	6100 ± 145	2.8	8
	(ii)	-0.42 ± 0.07	0.0026 ± 0.0005	5 ± 1	6130 ± 145	2.6	8
3C 303 west	(i)	-0.84 ± 0.08	18.2 ± 2.5	$< 2^a$	266 ± 8	0.31	9
	(ii)	-0.84 ± 0.07	11.5 ± 1.3	$< 2^a$	265 ± 8	0.37	9
3C 405 A	(i)	-0.51 ± 0.05	$0.09^{+0.10}_{-0.05}$	$40^{+20}_{-15}{}^b$	37300 ± 300	0.62	14
3C 405 D	(i)	-0.45 ± 0.05	$0.08^{+0.04}_{-0.02}$	$25^{+11}_{-9}{}^c$	49600 ± 500	0.46	14
3C 273 A	(i)	-0.60 ± 0.04	4.2 ± 0.3	290 ± 50	2110 ± 60	1.27	7
Pictor A west[d]	(i)	-0.740 ± 0.015	9.2 ± 0.2	< 2	2200 ± 20	0.66	10

[a] Deliberatly chosen since the solution is not unique, see text.
[b] The break frequency is well determined: ν_b = (5.5 ± 0.5) GHz.
[c] ν_b = (10.8 ± 1.0) GHz.
[d] Preliminary result, based on unpublished radio and K-band data.

rather reassuring.[2] Nevertheless, having available two independent measurements based on imaging data we ignore our old value in the spectral fits (Fig. 2c). As expected this leads to a slightly higher cutoff frequency (Table 5) than given in Paper I. As discussed in Paper I the radio flux from the source might be decomposed into a "pure" hot spot and the contribution from a parabola shaped ridge of the lobe. Since the extended parabola might well radiate synchrotron light (see Meisenheimer 1989, Crane & Stiavelli 1992) we will discuss in this Paper the spectrum of the entire source. Its power-law slope $\alpha_0 = -0.75$ is much steeper than in most other hot spots (see Fig. 3a) and resembles that found in the *jets* of M 87 and 3C 273.

3C 65. This radio source is identified with a galaxy at $z = 1.176$ and is the most distant member of our sample. The source has two bright hot spots (see the 5 GHz map of Longair 1977 and Table 4) The two hot spots are separated by 17 arcsecs and so could be imaged simultaneously. The galaxy itself is easily detected in our infrared image (Fig. 1d), but there is no obvious infrared emission from either of the hot spots. The only deep optical image of this source which encompasses the hot spots is that obtained by Gunn et al. (1981) at the Palomar 5m. The hot spots were undetected in their i-band image and we have used this non-detection to derive a rough estimate for the upper limit to the optical flux quoted in Table 3.

3C 111 East. This hot spot was detected in the infrared with the aperture photometer at UKIRT (Paper I) and is easily detected in our infrared image (Fig. 1e). A 1500s R-band image obtained at Calar Alto in October 1985 with the 3.5 m provided the optical measurement quoted in Paper I. The source has also been detected at 1.3mm by IRAM (Paper I). The reddening corrected K-band flux (111 ± 12 μJy) obtained from our earlier aperture photometry (via image reconstruction and subtraction of the bright star to the north-east) agrees well with the value that we obtain from our infrared imaging (105 ± 4 μJy). Accordingly, the spectral fits presented in Paper I are completely unchanged – albeit with a smaller error (Fig. 2d and Tab 5). The slightly smaller χ^2 value of the fit with a steep cutoff model (ii) is less significant than it appeared in paper I.

3C 123 East. The eastern hot spot of this source (component G on our 15 GHz VLA map shown in Paper I) is extremely bright in the radio and is characterised by its very high contrast with the surrounding radio emission. A deep R-band image obtained with the 3.5m at Calar Alto failed to provide an optical identification. A single scan was made with the infrared aperture photometer at UKIRT (Paper I) providing a limiting K-band flux of 39 μJy (3σ). Our new infrared imaging (Fig. 1f) does not constrain the upper limit to better than 72 μJy (5σ) due to the poor flat-field

[2] A further comparison between photometry obtained by image reconstruction of aperture measurements and our direct imaging is possible for 3C 111 E, which is discussed below.

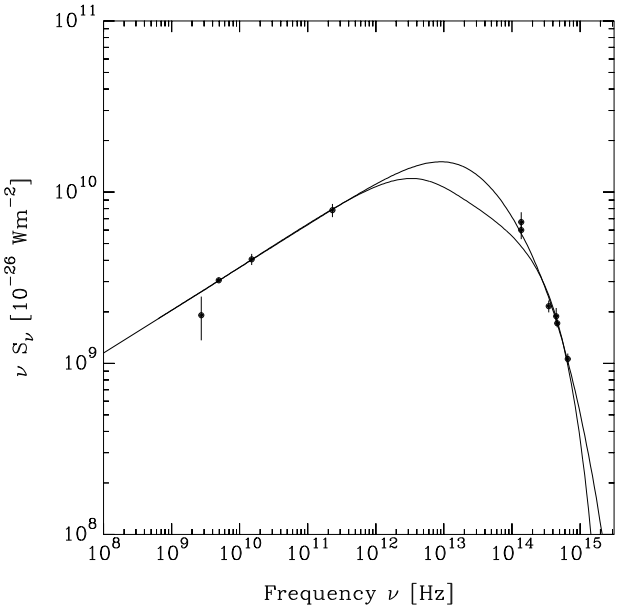

Fig. 2c. Spectrum of 3C 33 South (model fits as in Fig. 2a).

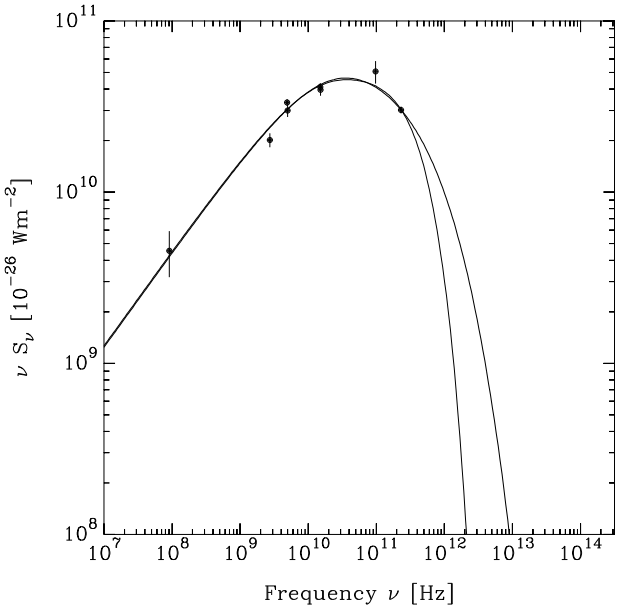

Fig. 2e. Spectrum of 3C 123 East (model fits as in Fig. 2a).

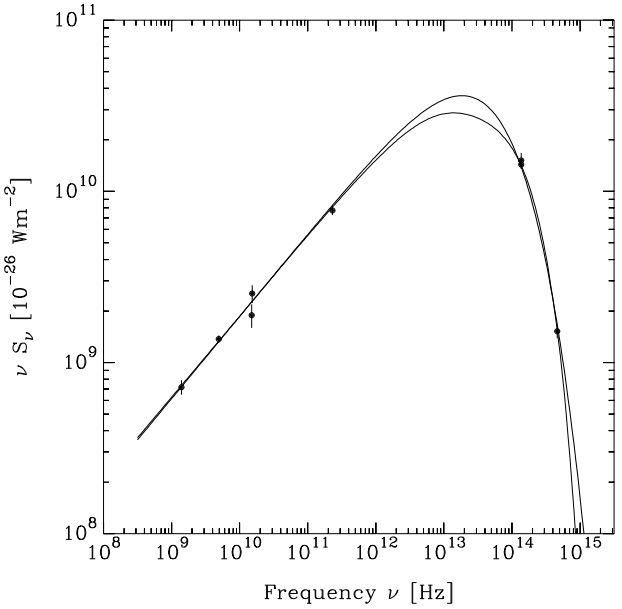

Fig. 2d. Spectrum of 3C 111 East (model fits as in Fig. 2a).

that was derived for this object since most of the field is covered by the radio galaxy. Although we have no detection in the infrared, the hot spot has been detected at 1.3mm (Paper I), and is by far the brightest that we have observed at this wavelength. A recent measurement at 3 mm (98 GHz, see Table 4) strongly favors the "minimum cutoff" spectrum already proposed in Paper I without an obvious break at radio frequencies. It is much better described by a straight power law $\alpha_0 = -0.45$ which cuts off at an unusually low frequency $\nu_c = 6 \times 10^{11}$ Hz. If there is a spectral break it has to lie somewhere beyond 15 GHz. (see Fig. 2e and Table 5). This spectrum predicts a K-band flux which lies orders of magnitude below the best sensitivities we reached in this work.

The large extent of the hot spot along the radio axis and a complicated field structure indicate that the simple one-dimensional model assumed in Paper I is not appropriate.

3C 303 West. The radio source associated with the 'N' galaxy 3 C303 is quite complex. The western lobe consists of two components, a high surface brightness hot spot (A in the nomenclature of Laing 1981) and a more diffuse component (B). The hot spot A is actually double (components A_1 and A_2 in the 408 MHz map of Lonsdale et al. 1983), A_2 being the brightest in the radio. Most of the polarized flux of the lobe comes from the fainter component A_2. A jet is emanating from the radio nucleus (very clearly shown in the 1.4 GHz map of Perley 1989), enters A_2 and ends in a low-surface brightness feature beyond the hot spot.

Early photographic imaging of the western lobe (Lelièvre & Wlérick 1975, Kronberg 1976) revealed the presence of three objects in the region of A, all with UV-excesses (denoted G, C and H in the nomenclature of the latter author). Object G coincides with A_2 to better than $2''$ and provided the first optical candidate for any radio hot spot. A spectrum of object G showed a faint, blue continuum and no emission or absorption features (Kronberg et al. 1977). Lonsdale et al. (1983) noted that a power-law connection between radio and optical emission of the the hot spot would have almost the same slope as the spectrum between 408 MHz and 5 GHz, thus leading to the suggestion that the optical emission is a direct extension of the synchrotron emission seen in the radio. We obtained R-band polarization observations of this hot spot (using the same instrumentation and observing procedures as for 3C 20, Hiltner et al. 1994). But the poor S/N-ratio of these data, together with the low polarization

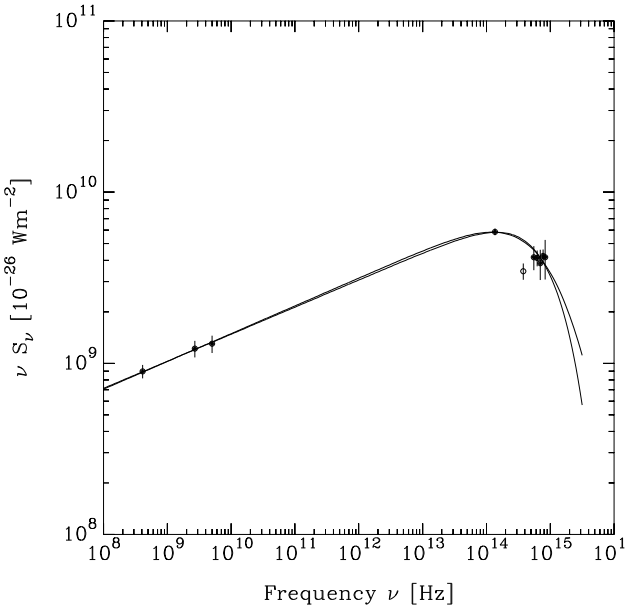

Fig. 2f. Spectrum od component A_2 in 3C 303 West (model fits as in Fig. 2a).

values expected for A_2 prohibited definite conclusion about the synchrotron nature of the light from object G.

The candidate optical counterpart G is easily detected in our infrared image (Fig. 1g). It shows exactly the double structure of A_2 orientated along PA $\simeq$ 140° which is known from the radio maps. In addition we detected a clear signal of the radio jet which connects the core (just outside the left boundary of Fig. 1g) with the hot spot. The object just to the south-west of the hot spot is a quasar at $z = 1.57$ (Kronberg et al. 1977). Table 3 shows the optical flux values of G obtained by Keel (1988) and Lelièvre & Wlérick (1975). We have flux calibrated the latter authors' data using the calibration of Hayes (1985). Although the large scatter of the optical data prohibit definite conclusions about the high frequency spectrum (see Fig. 2(f)) we think that both the steep radio-to-optical spectral index $\alpha_0 = -0.84$ and the high value of the cutoff frequency $\nu_c > 10^{15}$ Hz, as well as the detection of the radio jet qualify this hot spot candidate as bright knot in the jet, rather than a genuine radio hot spot. We therefore do not consider 3C 303 west in the general discussion of hot spot spectra (Section 4).

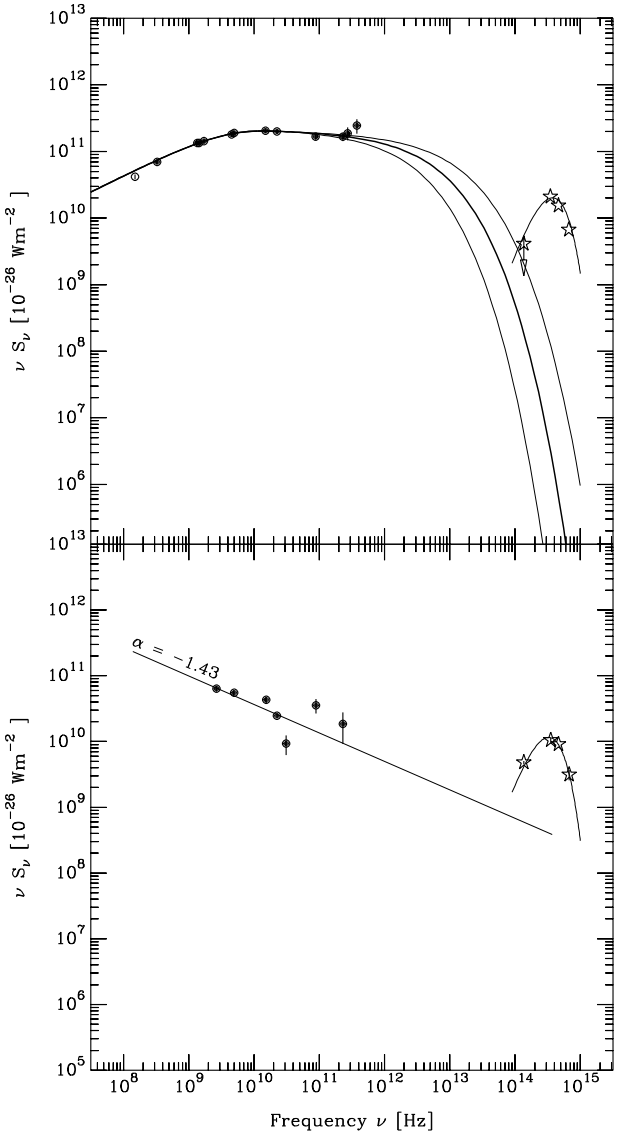

Fig. 2g. Spectra of the hot spots A and B in the western lobe of Cygnus A (3C 405). The optical counterpart of hot spot A is an K-star (flux values symbolized by stars). The millimetre spectrum together with the K-band upper limit confines the high frequency spectrum to the range between the thin lines. The best-fit spectrum is represented by a thick line. The optical counterpart of hot spot B is also an K-star. The steep power-law spectrum is not confined by the high frequency data.

3C 405 – Cygnus A. The hot spots in the lobes of the classical double radio source Cygnus A are by far the brightest known, and indeed Swarup et al. (1963) first identified the hot spot phenomenon in a discussion of this source. Hargrave & Ryle (1974) were prompted in a study of this source to suggest for the first time the need for a continuing particle acceleration in the hot spots themselves, although they did not discuss any mechanisms. We will use the nomenclature of their 5 GHz map in this present discussion. Both of the hot spots are double (Miley & Wade 1971) and there is some evidence that each consists of a primary hot spot connected by a tail of flat-spectrum, highly polarized emission to a secondary hot spot (Lonsdale & Barthel 1986, Carilli et al. 1989). The hot spots in the western lobe (components A and B) are together the brightest: B is the more compact of the pair (0.7 × 0.4 arcsec, Dreher 1981), but A is brighter in the radio. Both A and B have sharp leading edges (Linfield 1981).

Kronberg et al. (1977) obtained deep IIIa-J plates with the Palomar 5m and found that component B coincides with a stellar object ($J \simeq 22$) but there was no candidate for A (to $J \simeq 24$). Similarly no candidate for the brightest component of the eastern lobe (component D) was found. Given the low galactic latitude

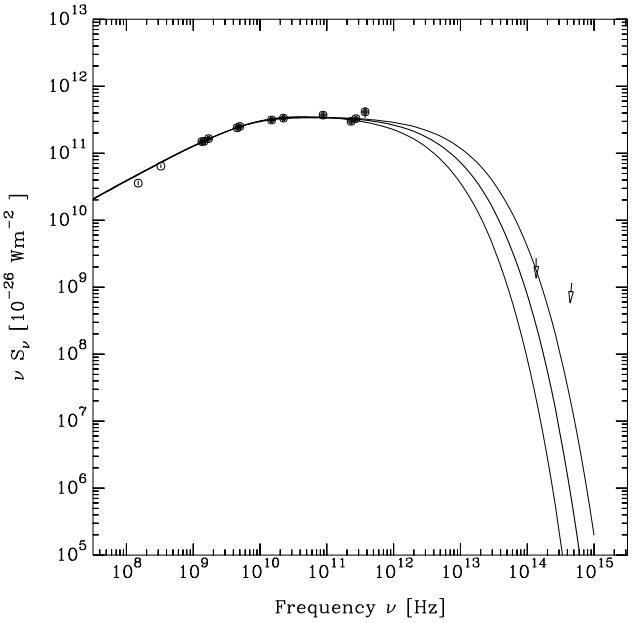

Fig. 2h. Spectrum of hot spot D in the eastern lobe of Cygnus A (3C 405). The millimetre spectrum together with the K-band upper limit confines the high frequency spectrum to the range between the thin lines. The best-fit spectrum is represented by a thick line.

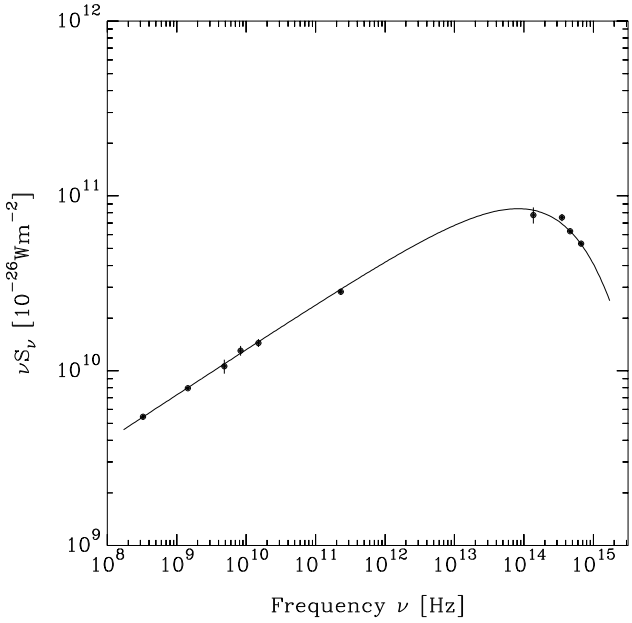

Fig. 2i. Spectrum of the hot spot in the western lobe of Pictor A (we thank Richard Perley for the permission to use the radio data before publication).

of Cygnus A ($b = 6^{\mathrm{o}}$), these authors prophetically commented on the possible chance coincidence of galactic objects with the hot spots, and furthermore, the sole optical candidate for B was offset by ≥ 1 arcsec in both RA and DEC from the radio emission. The original astrometry was subsequently improved (Kronberg et al. 1977: Erratum), leading to a good coincidence between hot spot B and its possible optical counterpart and a candidate near hot spot A. We confirmed the new astrometry on deep CCD images in three bands, B, R, I (Röser et al. 1995). However, no optical polarization could be detected for the candidate identification of hot spot B whereas the radio emission is highly polarized. The optical candidates for B and A are clearly detected on our K-band image (Fig. 1h). But the combination of our optical photometry (Table 3) with the K-band flux reveals that the spectra of both objects peak around $\lambda = 1\mu$m and cannot be regarded as the high-frequency continuation of the radio to millimetre synchrotron spectrum (Fig. 2g,h). On the other hand, blackbody spectra with T = 4000 K (candidate for B) and T = 4600 K (A), respectively, describe the near-IR/optical photometry quite well. So we conclude that both are foreground K stars. This also explains the lack of detectable optical polarization.

The coincidence of both hot spots with galactic foreground stars will prohibit the detection of their near-IR emission until the resolution is improved to the $0\farcs1$ level which should allow to separate the light from the stars. Nevertheless, from the fit of the blackbody spectra we reckon that in both cases the underlying hot spot cannot contribute more than half of the measured K-band flux. It is obvious from Fig 2g that the corresponding upper limit (corrected for galactic extinction) does not constrain the high frequency tail of hot spot B's synchrotron spectrum as a straight power-law extrapolation of the radio-millimetre spectrum passes below this limit. In the case of hot spot A, however, the K-band upper limit requires that the spectrum bends down somewhere between 10^{12} and 10^{14} Hz (Fig. 2h). Assuming a similar high frequency cutoff as observed in other radio hot spots (model (i)) the combination of a straight radio to millimetre spectrum and the upper limit at K constrains the position of the cutoff at $\nu_c = (9^{+10}_{-5}) \times 10^{12}$ Hz.

In the case of the dominant eastern hot spot D the situation is more clear-cut since neither our deep optical nor our K-band image show any object near the hot spot position (Fig. 1h). Again the upper limit at K provides the most stringent constraint on the high frequency spectrum (Fig. 2h). Assuming the standard cutoff spectrum (model (i)) places the cutoff at $\nu_c = (8^{+4}_{-2}) \times 10^{12}$ Hz.

Thus, due to their very high millimetre flux, the upper limits from our K-band images are already sufficient to constrain the cutoff frequency in the spectra of the brightest hot spots A and D to better than a factor of 2. While presumably hot spot A will remain hidden behind the foreground K-star, it should be possible to detect the near-IR counterpart of hot spot D (best-fit expectation: $\mathrm{K} = 21\fm3$) on a very deep image with state of the art NIR arrays.

Both hot spots show spectra which are nicely fitted by a $\Delta\alpha = 0.5$ break. This was already demonstrated by Carilli et al. (1991). Knowing the overall synchrotron spectrum, however, enables a more complete description of the physical parameters than was possible from the break in the radio spectrum alone (see Roland et al. 1988).

It is curious to note that both hot spots of Cygnus A, which in many respects has served as *the* example for radio galaxies

in general, show low frequency power-law slopes $\alpha_0 \simeq -0.5$, that is exactly the value which is predicted by first order Fermi acceleration at a strong non-relativistic shock front (Bell 1978).

Recent ROSAT observations of Cygnus A (Harris et al. 1994) detected both dominant hot spots (A,D) at frequencies beyond 10^{17} Hz. The authors favour a synchrotron-self-Compton origin of the X-rays from which they derive hot spot magnetic field of 16 and 25 nT for hot spots A and D, respectively.

Pictor A West Although the western hot spot of Pictor A could not be observed in the present work due to its southern declination we have to mention that recent K-band imaging has proven our original near-IR photometry to be erroneous. Thus the unexplained discrepancy between the optical and near-IR spectrum (see e.g. Fig. 6 in Paper I) has disappeared and the spectrum can be well described by a power-law spectrum with a high frequency cutoff at $\nu_c = 9 \times 10^{14}$ Hz (see Fig. 2(i), more details will be given in Röser et al. 1997). Based on better radio maps of Pictor A (Perley et al. 1997) we rule out any break in the GHz regime but find that a rather steep power-law ($\alpha_0 = -0.74$) extends from 1 GHz to the high frequency cutoff. The much improved radio-to-optical spectrum definitely rules out the speculation by Röser & Meisenheimer (1987) that the synchrotron spectrum extends straight into the X-ray regime. Thus the extraordinary bright optical hot spot in Pictor A west (the only one which has been so far detected above the limit of the POSS plates on the ESO quick blue survey) is not caused by an extraordinary spectrum but by a cutoff frequency which is slightly higher than that typical of optically detected hot spots (see Table 5 and Fig. 4b). As in Cygnus A the X-rays are presumably caused by the Synchroton-Self-Compton effect or thermal Bremsstrahlung of the hot plasma near the working surface of the jet.

The best resolved radio maps of Pictor A west (Perley et al. 1997) show that the hot spot displays a sandwich structure orientated perpendicular to the jet axis. The subcomponents cannot be resolved with $0\farcs15$ resolution. The axial width of the entire structure is $0\farcs4$, which gives a morphological orientation angle $\theta_{\rm morph}$ which is so close to the polarimetric angle $\theta_{\rm pol}$ that only an upper limit $L < 0.1$ kpc can be given for the axial extent of the brightest emission region. But it should be kept in mind that both the full radio and the optical emission region is distributed over > 1 kpc along the jet axis (Perley et al. 1997, Thomson et al. 1995).

4. Discussion

Although no new high frequency counterpart of any radio hot spot could be found in the present work we are able to extend the scope of Paper I considerably: We improved the spectra of 3C 20 and 3C 33. The upper limits to the K-band flux for the bright hot spots A & D in Cygnus A enable us to derive rather reliable synchrotron spectra which constrain the high frequency cutoff to a factor of 2. In addition, new millimetre and K-band measurements of 3C 123 and Pictor A have sorted out the ambiguities in the overall spectra which were present in our earlier work (Paper I). Likewise, new optical and K-band photometry of the terminal hot spot in the jet of 3C 273 has led to a reliable overall spectrum (Meisenheimer et al. 1996b) which we include for completeness in Table 5 and the present discussion.

Altogether we can base our updated discussion of the overall spectra of radio hot spots on 8 cases: The hot spots in 3C 20 W, 3C 33 S, 3C 111 E, 3C 123 E, 3C 273 A, 3C 405 A, D (Cygnus A) and Pictor A west. Although the improvement in number might not seem significant, the improvement in quality (6 out of the 8 hot spots have much better determined spectra) makes a revision of the discussion presented in Paper I mandatory. Moreover we feel that the detection of optical or near infrared synchrotron radiation from locations well outside prominent hot spots or knots is so striking that it no longer can be ignored (as we did in Paper I).

Therefore, we divide the following discussion into three parts: In the first paragraph (4.1) we will apply the standard Fermi acceleration model for the synchrotron spectra of radio hot spots (along the lines of Paper I). In 4.2 we will discuss the obvious shortcomings of the standard scenario before in the final part (4.3) we will try to summarize what the diversity of hot spot spectra could tell us about the physical processes which make the hot spots shine so brightly in the radio and sometimes even at optical frequencies.

4.1. Fermi acceleration models for radio hot spots

The standard model of particle acceleration in radio hot spots assumes diffusive shock acceleration (first-order Fermi acceleration) in which the relativistic electrons are accelerated by multiple scattering across the velocity jump of a strong shock front. Such a shock (Mach disk) is expected to exist in the working surface of supersonic jets. In Paper I we pursued this standard model in great detail in order to explore whether it leads to a self-consistent description of the particle spectra (as inferred from the observed synchrotron spectrum) and other parameters like size and shape of the hot spot emission region, magnetic field strength and the speed of the inflowing jet plasma. We concluded that self-consistent solutions can be found for all 6 hot spots contained in Paper I and presented a rather detailed set of physical parameters for them (see Table 5 and Figs. 8 and 9 in Paper I). Thus our first objective is to check our former results on the basis of the improved spectra for these 6 hot spots and the inclusion of the two bright hot spots of Cygnus A for which we could determine the spectra. In this section we derive the physical parameters exactly in the same way as outlined in Paper I. Thus the parameters summarized in Table 6 can directly be compared with those of Paper I.[3]

In Paper I we identified two distinct types of hot spot spectra:

(A) *low loss* hot spots which are characterized by their low frequency power law of rather flat slope ($\alpha_0 \simeq -0.5$) extending out towards high frequencies ($\nu > 10^{12}$ Hz) where the spectra turn down in a high frequency cutoff.
This is in remarkable contrast to the spectra of

[3] *Erratum:* The expressions for P_{acc} and ϵ_{acc} in Paper I contained an erroneous $I_\gamma - 1$ instead of just I_γ.

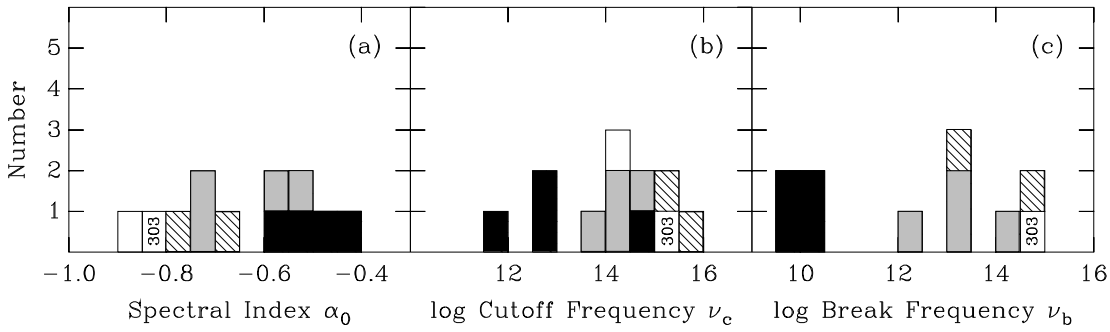

Fig. 3a–c. Distribution of fit parameters for the hot spot spectra: **a** Low frequency spectral index α_0, **b** cutoff frequency ν_c, **c** break frequency ν_b. The grey shading indicates low loss hot spots, the black shading high loss hot spots, the diagonal hatching the brightest knots in the jets of M 87 and 3C 273, and the open box the eastern lobe in M 87, respectively. The optical counterpart in 3C 303 west is labelled "303".

(B) *high loss* hot spots in which the flat spectrum ($\alpha_0 \simeq -0.5$) extends only to around 10^{10} Hz where it bends by $\Delta\alpha$ = 0.5 before the cutoff at around 10^{14} Hz is reached. Such a $\Delta\alpha$ = 0.5 break is naturally expected if the electrons which have been accelerated in the shock front lose most of their energy within a hot spot emission region which extends downstream of the shock over several hundred or thousand times the electron mean free path λ_e (Heavens & Meisenheimer 1987).

The low and high loss hot spots are shown in Figs. 3, 4 & 5 by a gray and black shading, respectively.

Since the spectra of the three low loss hot spots from Paper I (3C 20 west, 3C 33 south, 3C 111 east) have been refined only marginally our previous results hold unchanged. The main difference concerns 3C 33 south, the complex emission region of which we treat here as a single source, rather than a two component object as in Paper I. Therefore our one-dimensional model is not strictly applicable and several parameters in Table 6 are only of qualitative nature (see also Section 4.2).

The most substantial adjustments have to be made for the hot spots in 3C 123 east and Pictor A west since their spectra are changed considerably by new flux measurements: The best fit spectrum of 3C 123 east is now definitely characterized by a high frequency cutoff in the millimetre range which makes the $\Delta\alpha$ = 0.5 break rather inconspicuous although our model fits still place the break frequency as low as $\nu_b = (13 \pm 3)$ GHz. So our classification of 3C 123 E as a high loss hot spot remains valid, despite the fact that γ_c/γ_b is an order of magnitude below the upper limit in Paper I. The complicated structure of this hot spot has not been disentangled by any better radio maps. Thus the physical parameters in Table 6 are again only qualitative.

Due to better radio data and the correction of the erroneous NIR photometry, the spectrum of Pictor A west has been altered completely: The lack of any low frequency break classifies this hot spot now as *low loss* type, albeit with a very steep power law slope $\alpha_0 = -0.74$. As in 3C 33 south this fact and the largely extended radio *and* optical emission region makes the application of the standard model rather dubious. Even if we apply the model only to the thin sheet (filament ?) of highest surface brightness at the leading edge of the hot spot we get a large discrepancy between B_+ and B_{me} indicating that the model assumptions fail.

Notwithstanding the fact that new NIR photometry of the leading hot spot 3C 273 A of the jet of 3C 273 (Neumann et al. 1996), together with the optical data published in Röser & Meisenheimer (1991) allows us to determine the high frequency shape of its spectrum with much superior accuracy (Meisenheimer et al. 1996b), the essential conclusions of Meisenheimer & Heavens (1986) which were included in Paper I remain unchanged: The $\Delta\alpha$ = 0.5 break at GHz-frequencies is confirmed and the high frequency cutoff can be accurately pinned down at $\nu_c = 4 \times 10^{14}$ Hz (see Table 5). Moreover, the positional offset between the mean radio emission and the optical peak which is predicted in the model of synchrotron losses in a finite downstream emission region (Meisenheimer & Heavens 1986) seems to be confirmed by a recent comparison between a radio maps and HST images (Röser et al. 1996). So we are rather confident that the model applies to this source and the parameters given in Table 6 are reliable.

Applying our model to the brightest hot spots in Cygnus A which both have well defined low frequency breaks by $\Delta\alpha$ = 0.5 and a measurable length L of their downstream emission region leads to an equally self-consistent sets of parameters. We regard this as further evidence that the basic concept of a thin acceleration region (presumably at a strong shock) which is followed downstream by an extended emission region is sensible. It is interesting to note that in all three well defined high loss hot spots we derive a mildly relativistic inflow speed $v_j \simeq 0.25\,c$ which is at the lower end of the distribution in Fig. 4b. This might be due to the fact that all these hot spots should be classified as "secondary hot spots" in the sense that they have a more compact precursor in which the jet might be slowed down considerably. The wide spread of v_j in low loss hot spots might be due to large uncertainties in both the length L and γ_c/γ_b. The "true" distribution may well be consistent with $v_j \lesssim 0.5\,c$.

If we ignore the aforementioned difficulties in applying the simple shock acceleration model to some hot spots with complicated structure we still find a rather self-consistent picture: In general, the minimum energy field estimate B_{me} and that from the downstream losses B_+ agree within the errors. The (aver-

Table 6. Physical conditions in the hot spot emission regions.

	3C 20 west	3C 33 south	3C 111 east	3C 123 east	3C 273 A	3C 405 A	3C 405 D	Pic A west
Redshift z	0.174	0.0595	0.0485	0.2177	0.158	0.0565	0.0565	0.0350
Scale [kpc/arcsec]	4.0	1.59	1.31	4.7	3.7	1.51	1.51	0.97
Angle to L.O.S. $\theta_{morph},\ \theta_{pol}$	44.7, 55.	44.7, 46.	57.6,56.3	?	41.4, 46.	53.,60.	50.,60.	66.5,68.
Hot spot Diameter D [kpc]	0.76 ± 0.04	2.40 ± 0.20	1.99 ± 0.03	5.	2.2 ± 0.7	2.9 ± 0.3	2.1 ± 0.3	0.97 ± 0.03
Hot spot Length L [kpc]	0.13 ± 0.08	0.08 ± 0.04	0.07 ± 0.07	4.	1.9 ± 0.7	1.5 ± 0.3	1.4 ± 0.3	0.05 ± 0.05
Total Luminosity P_{syn} [10^{36} W]	7.2	1.53	1.30	43.7	13.5	28.2	40.0	2.40
Min. Energy Field B_{me} [nT]	65^{+20}_{-08}	30^{+7}_{-4}	31^{+18}_{-9}	23 ± 3	35^{+8}_{-4}	35 ± 3	41 ± 3	59^{+35}_{-11}
Downstream Field B_+ [nT]	36^{+25}_{-10}	21^{+12}_{-05}	18^{+35}_{-9}	16 ± 4	39^{+24}_{-10}	47^{+8}_{-5}	41^{+8}_{-5}	21^{+40}_{-10}
Best-guess parameters:								
Magnetic Field B_{HS} [nT]	48	25	24	19	36	40	41	35
Minimum Presure [nPascal]	0.72	0.20	0.18	0.11	0.41	0.50	0.51	0.37
Max. Energy $\gamma_c = E_c/m_e c^2$	2.6×10^5	5.5×10^5	2.9×10^5	3.0×10^4	5.7×10^5	7.5×10^4	7.0×10^4	8.1×10^5
Acceleration Time $\tau_{acc}(\gamma_c)$ [yr]	330	430	1200	20600	290	1950	2200	150
Shock acceleration model:								
Compression Ratio r	3.7	(3.0)	3.8	4.3	3.5	3.9	4.3	(3.0)
Upstream Jet Speed $u_j = v_j/c$	0.47	(0.39)	0.35	0.40	0.27	0.24	0.30	(0.66)
Mean Free Path $\lambda_e(\gamma_c)$ [pc]	4.6	(4.6)	7.8	190.	1.4	6.8	11.3	(4.8)
Flux of relativ. e^- j_0 [$\mathrm{m^{-2}s^{-1}}$]	1.5×10^9	2.3×10^8	4.9×10^7	1.0×10^8	1.9×10^8	4.7×10^7	9.3×10^7	6.5×10^9
Min. Flux of p^+ j_p [$\mathrm{m^{-2}s^{-1}}$]	3.1×10^9	1.4×10^9	6.9×10^8	5.5×10^8	3.1×10^9	4.2×10^9	3.4×10^9	1.1×10^9
Max. Fraction $\eta_{rel} = j_0/j_p$	0.49	(0.23)	0.07	0.18	0.06	0.02	0.03	(5.8)
Max. Synchrotron Efficiency ϵ_{syn}	0.33	0.03	0.07	0.39	0.22	0.25	0.51	0.09
Max. Acceleration Efficiency ϵ_{acc}	0.73	(0.77)	0.52	0.61	0.38	0.30	0.55	(3.5)

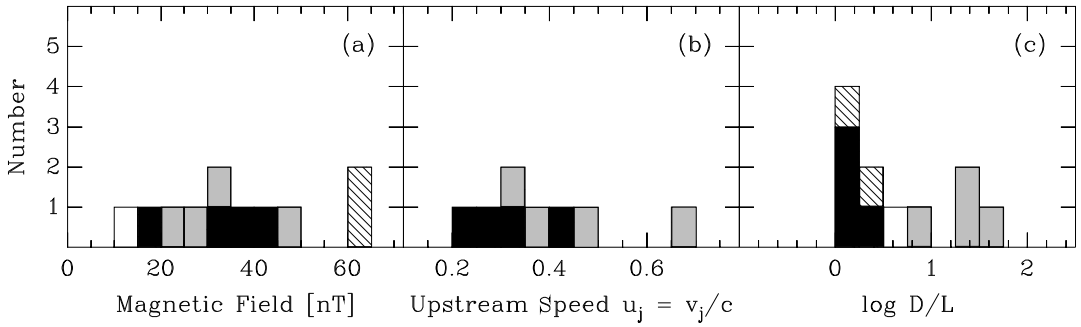

Fig. 4a–c. Distribution of derived hot spot parameters: **a** Best-guess magnetic field B_{HS}, **b** jet speed upstream of the hot spot $u_j = v_j/c$, **c** geometric parameter D/L. Shading as in Fig. 3.

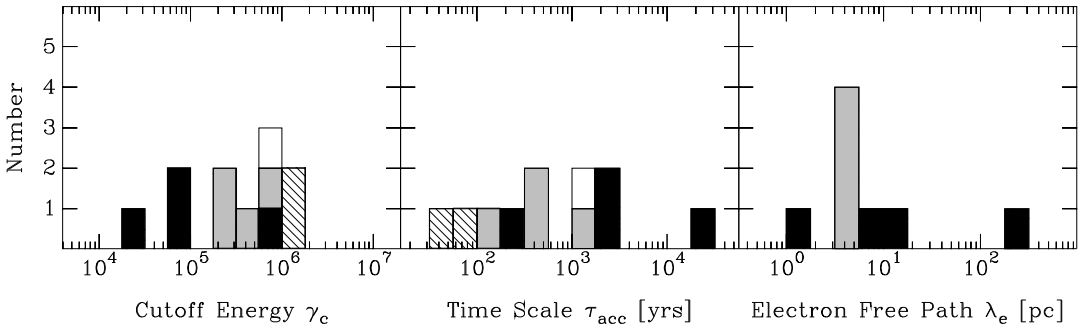

Fig. 5a–c. Distribution of parameters concerning the particle acceleration in hot spot: **a** Maximum energy $\gamma_c = E_c/m_e c^2$, **b** acceleration time scale τ_{acc}, **c** electron mean free path λ_e. Shading as in Fig. 3. The three high loss hot spots with $\gamma_c < 10^5$, $\tau_{acc} > 1000$ yrs, and $\lambda_e > 5$ pc are not detected in either the K-band or the optical.

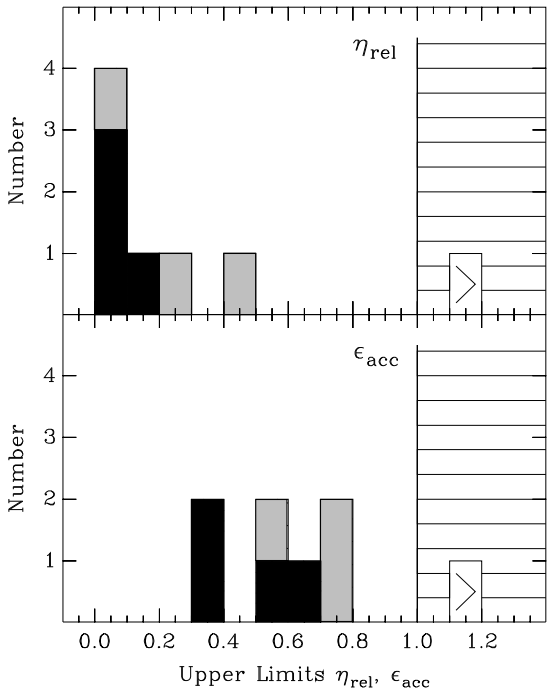

Fig. 6a and b. Histogram of **a** the maximum fraction of electrons with relativistic energies η_{rel}, and **b** maximum required acceleration efficiency ϵ_{acc}. Shading as in Fig. 3. Note that only one hot spot, Pic A west lies in the forbidden area $\eta_{rel} > 1,\ \epsilon_{acc} > 1$.

aged) *best guess* magnetic field values cluster quite narrowly around B_{HS} = 30 nT (Fig. 4a). This means that the large spread of observed cutoff frequencies $6 \times 10^{11} < \nu_c < 10^{15}$ Hz is mainly caused by a comparable spread in maximum energies $3 \times 10^4 < \gamma_c < 8 \times 10^5$. Within the shock acceleration model this has to be assigned to a rather wide distribution of acceleration time scales τ_{acc} which are determined by the mean free path of the electrons λ_e (or the diffusion coefficient). However, it is interesting to note that in both the distributions of the magnetic field strength and that of the maximum energy γ_c the hot spots seem to be overtaken by the brightest knots of optical jets. Maybe the hot spot phenomenon is not as outstanding as hydrodynamic jet simulation suggest and resembles the "normal" knots in the jet flow.

As emphasized in Paper I the most important consistency check of the shock acceleration model considers whether the number of relativistic electrons $n_{rel}(\gamma_0, \gamma_c)$ (between a "cut-on" energy γ_0 and the maximum energy γ_c) is only a (small) fraction of the total number of electrons in the jet flow, and whether the energy injected into relativistic electrons at the shock P_{acc} can be provided by the kinetic energy flux of the jet P_{kin}. As the jet's ram pressure has at least to balance the minimum pressure in the hot spot, the estimate for v_j gives a handle to set a lower limit to the incoming proton and kinetic energy flux. Thus the model sets upper limits to the required fraction of relativistic electrons $\eta_{rel} \equiv n_{rel}/n_p$ (assuming a neutral ep-jet: $n_e = n_p$) and to the acceleration efficiency $\epsilon_{acc} \equiv P_{acc}/P_{kin}$. The upper limits for η_{rel} and ϵ_{acc} derived from our *best guess* parameter set are given at the bottom of Table 6 and visualized in the histograms of Fig. 6a,b. Obviously only one of the two hot spots with the outstanding steep low frequency spectra $\alpha_0 \simeq -0.75$ (Pictor A west) is in conflict with the requirement $\eta_{rel} < 1$ and $\epsilon_{acc} < 1$ (3C 33 south is no more extreme than 3C 20). This conflict could be solved by assuming a higher "cut-on" frequency $\gamma_0 \gtrsim 500$ (instead of the standard value γ_0 = 100 we assumed here). But together with the other morphological and spectral evidence pointing away from the standard model we think it is highly unlikely that such a fine tuning could save the simple shock acceleration scenario for the extended hot spots of 3C 33 and Pictor A.

At this point, we should emphasize that the high frequency spectra of both the high- and low-loss hot spots are very well described by our simple one-dimensional model which essentially assumes a *constant* down-stream magnetic field. On the other hand, one might expect that the complicated flow pattern in the hot spot region (e.g. Kössl et al. 1990) should produce wide variations in the *local* magnetic field strength and thus "smear out" the cutoff spectrum which we derived from the idealized field geometry. The observed lack of this "smearing out" effect can be understood as follows: In the observed frequency range (just above the cutoff frequency ν_c) the typical spectral index is $\alpha_{opt} \lesssim -2$. Accordingly, the mean emissivity (per unit volumn) is a strong function of the local magnetic field: $\epsilon_\nu \propto B^{1-\alpha} \simeq B^3$ or steeper. Thus those parts of the hot spot with the highest magnetic fields will dominate the spectral shape around ν_c. A significant smoothing of the spectrum could only occur if the total emission region is much larger than the acceleration region (near the shock). However, model calculations which take into account both a wide variety of field geometries (i.e. including fields the strength of which decline rapidly away from the shock) and a proper treatment of the synchrotron losses result in spectra which always show the low-loss or high-loss characteristics without significantly changing the shape around ν_c. Only with a very carefull balance of declining field strength and synchrotron losses it is possible to alter the shape of the high frequency spectrum. But these solutions are only possible in a hot spot region without sharp boundaries. If the volumn which contains the widely varying field is limited the dominance of the regions with the highest magnetic field inevitably determine the spectra.

In summary, we conclude that first-order Fermi acceleration at a strong, non-relativistic shock can well account for the observed properties of 6 out of the 8 hot spots in our sample. The major arguments which support this are:

(a) The low frequency spectral indices lie exactly in the range $-0.6 < \alpha_0 \lesssim -0.45$ which is predicted for mildly relativistic shocks (Bell 1978, Ballard & Heavens 1991).
(b) The independent magnetic field estimates B_{me} and B_+ (from downstream losses) agree for mildly relativistic jet speeds $0.2\,c < v_j \lesssim 0.5\,c$.
(c) Both the fraction of relativistic electrons η_{rel} and the acceleration efficiency ϵ_{acc} lie comfortably below 1.

(d) Emission regions appear longer (along the jet axis) in high loss hot spots while they seem to be thin sheets in low loss hot spots.
(e) The only source for which a comparison between the radio and optical morphology is available at the required resolution $\ll 1''$, 3C 273 A shows exactly the predicted offset between its optical peak ($\nu_{obs} \simeq \nu_c$) and the radio hot spot (at $\nu_{obs} = 1.7\,\mathrm{GHz} < \nu_b$).

The obvious counter-examples, the hot spots in 3C 33 south and Pictor A west, fail to show more than two of the properties (a) – (e).

4.2. Limitations of the Fermi acceleration model

In the present sample the most obvious conflict with the standard shock acceleration model occurs in the hot spots of 3C 33 south and Pictor A west, both of which show a steep power law index $\alpha_0 \simeq -0.75$ and an optical emission region clearly extending beyond a sheet or disk which would be expected for shock acceleration where the acceleration region should extend no more than a few mean free paths λ_e (see Table 6) from the major velocity jump. The most striking example for extended synchrotron light is found near the hot spot of Pictor A west, in which a filament stretches out by > 5 kpc on either side of the jet. We think that this evidence for widely distributed particle acceleration has to be seen in the context of the finding that the optical emission from radio jets is also not confined to bright, individual knots but follows the radio morphology very closely (Meisenheimer 1991, Boksenberg et al. 1992, Meisenheimer et al. 1996a).

The detection of the radio jet in 3C 303 together with the clearly extended morphology of the hot spot on our K-band image (Fig. 1(g)) indicates that this object belongs into the same category.

But extended optical emission is not the only evidence for particle acceleration taking place outside hot spots and bright knots. Even in the case of the well established high loss hot spots in 3C 273 and Cygnus A there is a problem: We have determined the break frequency ν_b and thus the maximum energy with which the electrons leave the hot spot downstream. Even if the magnetic field strength in the lobes surrounding the hot spot is comparable to that in the hot spot (which is not supported by minimum energy estimates of the field, see e.g. Carilli et al. 1991) the lobe spectra should not extend beyond ν_b if indeed the particle acceleration is done in the hot spots only. But the lobe spectra of Cygnus A extend well beyond 30 GHz (i.e. $\gtrsim 3\,\nu_b$) near the edges of the radio source (see Carilli et al. 1991, Meisenheimer 1996) and the extended radio "halo" around the hot spot in 3C 273 A seems to be visible on a deep K-band image (Neumann, 1995). So either the magnetic field is significantly enhanced over minimum energy in the lobes or additional acceleration is required outside the main shock.

Therefore, we would like to suggest the following generalization for *in situ* particle acceleration in extragalactic radio sources: There exists an acceleration mechanism in highly magnetized plasma which is not directly coupled to strong shocks but may work everywhere where shear or turbulence in the plasma flow generate strong magnetic fields. Although there is still little observational evidence how this process works in detail we tend to link its occurence to electro-magnetic plasma processes like reconnection and/or the generation of strong electric currents. This acceleration mechanism has to be mainly responsible for the very efficient particle acceleration which is required to explain the continuous emission of synchrotron light in optical jets (M 87, 3C 273, PKS 0521-36 and others). Therefore we will refer to it as "jet-like" acceleration. It generates rather step power-law spectra $-0.65 \gtrsim \alpha_0 \gtrsim -0.9$ and can reach very high energies ($\gamma_c > 10^6$).

At the strong shock (Mach disk) in the working surface of a supersonic jet the "jet-like" acceleration is either substituted or resembles the standard diffusive shook acceleration mechanism (Bell 1978). This leads to the "standard" shock acceleration spectra with slope $\alpha_0 \simeq -0.5$ observed in most hot spots. However, our observations of "broken" high-loss spectra in 3C 273 A and Cygnus A (hot spots A & D) which indicate an extended downstream emission region dominated by synchrotron losses (without re-acceleration) pose a severe problem to this concept of two distinct acceleration processes: Synchrotron losses can only dominate if the efficiency of the "jet-like" acceleration is un-important or quenched for some range down-stream of a strong shock. One may speculate that this could be caused by a "change of state" when magnetized plasma passes a strong shock. Moreover, further down-stream (e.g. in the lobes) the plasma seems to regain its ability to support jet-like acceleration in order to boost the maximum electron energy well above the value which is inferred from the losses within the hot spot (see also Meisenheimer 1996). We tendatively identify this effect with some kind of "magnetic tension" in jet-like plasmas which is relaxed within strong shocks but can subsequently build up again by the strong velocity shear and turbulence expected near the "contact discontinuity" between radio plasma and shocked outer material. If correct this interpretation would imply that velocity shear or turbulence are the prime movers of "jet-like" acceleration while a more ordered velocity jump or gradient leads to the classical shock acceleration spectrum. The relative importance of shock and jet-like acceleration in hot spots may depend on the distance between the Mach-disk and the contact discontinuity, which seems to be rather transient in numerical simulations of jets (see e.g. Kössl et al. 1990). Somewhat against intuition, the highest electron energies seem to be reached in those hot spots in which the jet-like acceleration dominates (Pictor A (west) and 3C 33 south), making them the optically brightest hot spots detected so far.

4.3. General results

The analysis of our sample of those 8 hot spot spectra, which are accurately determined by this work, strongly suggests that the emission of synchrotron *light* ($\nu \geq 10^{14}$ Hz) is only possible if maximum electron energies reached by the acceleration process exceed $\gamma_c > 10^5$. The second parameter that determines the maximum observed frequency – the magnetic field strength

B_{HS} seems to play a minor role since all hot spots in our sample (including those with $\nu_c < 10^{12}$ Hz) show essentially the same value $B_{HS} \simeq 30$ nT.

Independent of the acceleration mechanism, the energy γ_c will essentially be set by the balance of synchrotron losses and acceleration gains, i.e. $\tau_{loss}(\gamma_c) = \tau_{acc}(\gamma_c) = \frac{\gamma_c}{d\gamma/dt}$. From the observed cutoff frequency ν_c and the magnetic field in the acceleration region one can directly calculate τ_{loss} and thus gets τ_{acc} for any underlying acceleration process. It is obvious from Fig. 5b that acceleration time scales of $\lesssim 500$ years are *the* essential parameter to make a hot spot optically visible.

It is still unclear which physical parameter or process sets the time scale τ_{acc}. But we have presented here some more hints that nature has found at least two ways for effective particle acceleration: One process is identical or closely related to the standard concept of diffusive shock acceleration (Bell 1978). It produces an electron spectrum $N(\gamma) \sim \gamma^{-q}$ with a slope $q \simeq 2$, for which we find evidence in 6 of our 8 hot spots. Under favorable conditions an acceleration times scale of $\tau_{acc} \lesssim$ 300 yrs can be reached (but this seems to be rare since there are tens of radio hot spots which are bright enough in the radio to be optically detectable if $\nu_c > 10^{14}$ Hz).

The second process which is capable to reach $\gamma_{max} > 10^5$ does not seem to be confined to strong shocks but could work everywhere in highly magnetized plasmas. Its existence is required in order to explain the constant electron spectrum in the jet of M 87 (Meisenheimer et al. 1996a) but it also has to be at work in hot spots with very extended optical emission regions ($d \gg 1$ kpc). It is characterized by rather steeper electron spectra ($q \simeq 2.5$) and high acceleration efficiency ($\tau_{acc} < 100$ yrs) up to extremely high energies ($\gamma = 10^6$ or more).

5. Conclusions

We have obtained infrared K-band imaging of 11 hot spots in the lobes of powerful radio galaxies. We have detected infrared counterparts for three hot spots (3Cs 20W, 33S, 111E) which have known optical counterparts. The optical candidate in the western lobe of 3C 303 was also detected and shows a K-band morphology which resembles the radio morphology of the southern subcomponents. The K-band detection of the radio jet and the steep radio-to-optical spectrum of the hot spot complex point to it being the brightest knots in the jet rather than a genuine hot spot. Two hot spots in the powerful radio source Cygnus A (3C405) are found to be confused by galactic stars (hot spots A and B) and the third hot spot (D) was undetected. No infrared counterparts were found for the hot spots 3C 20 E, 65, and 123 E. We have used these detections and the upper limits for the brightest hot spots in Cygnus A to derive the overall synchrotron spectra from radio to optical frequencies.

Adding in the results for the leading hot spots of 3C 273 A and Pictor A (west) we now have collected reliable synchrotron spectra for 8 hot spots. Six of them show typical hot spot spectra which are characterized by a low frequency power-law $-0.45 \geq \alpha_0 \geq -0.60$ and a high frequency cutoff in the range $3 \times 10^{11}\mathrm{Hz} < \nu_c < 4 \times 10^{14}\mathrm{Hz}$, that is well below the value found in the optical counterparts of radio jets (Meisenheimer et al. 1996a,b). Three of them (3C 273 A, Cygnus A, hot spots A & D) show clear evidence for a spectral break by $\Delta\alpha \simeq 0.5$ in the radio regime ($\nu_b \simeq 10$GHz) which is expected if a thin acceleration region (strong shock) is followed by an extended downstream emission region in which synchrotron losses dominate (Heavens & Meisenheimer 1987). In all six cases the standard scenario of diffusive shock acceleration at the strong terminal shock provides a self-consitent description even for mildly relativistic jet speeds $0.2c \leq v_j \lesssim 0.5$.

However, the steep and over a wide area constant synchrotron spectra found in 3C 33 S, 3C 303 W and Pictor A (west) cannot easily be understood in this popular model. In addition, these hot spots exhibit exeptionally high cutoff frequencies $\nu_c \simeq 10^{15}$ Hz which place them right in the middle of the distributions of spectral indices and cutoff frequencies observed in optically detected radio jets. The extraordinary spectra and the absence of any indication of synchrotron ageing in these hot spots led us to the speculation that there exists a second "jet-like" acceleration process which is responsible for the synchrotron spectra of both optical jets and optically extended radio hot spots. The latter acceleration process has to be very efficient (typical acceleration time scale $\tau_{acc} \lesssim 100$ years around $\gamma = 10^6$) in order to replenish the particle energy losses almost "on the spot". Although its physics is completely unkown at present, we feel that a better understanding of particle acceleration and synchrotron spectra of extended radio source in general will be impossible unless we have an idea how this new process works.

Acknowledgements. We are grateful for the excellent support that we received at UKIRT during our observing run. Special thanks for service observations. K.M. would like to thank the Royal Observatory, Edinburgh for its kind hospitality which helped much in finishing this work. This is especially true for many discussions with Alan Heavens.

References

Alexander, P., Brown, M.T. & Scott, P.F., 1984, MNRAS 209, 851
Ballard, K.R. and Heavens, A.F. 1991, MNRAS 251, 438
Bell, A.R. 1978, MNRAS 182, 147
Biretta, J. A. and Meisenheimer, K. 1993, H.-J. Röser and K. Meisenheimer (eds.): *Jets in Extragalactic Radio Sources*. Lecture Notes in Physics Vol. 421, Springer Heidelberg, p. 159
Blandford, R.D. & Rees, M.J., 1974, MNRAS 169, 395
Burstein, D. & Heiles, C., 1982, AJ 87, 1165
Carilli, C.L., Dreher, J.W. & Perley, R.A., 1989, *Hot spots in Extragalactic Radio Sources*, p.51, eds Meisenheimer, K. & Röser, H.-J., Springer, Berlin
Carilli, C.L., Ulvestad, J., Dreher, J.W. & Leahy, J.P., 1991, ApJ 383, 554
Cowie, L.L, Gardner, J.P., Lilly, S.J. & McLean, I., 1990, ApJ 360, L1
Crane, P. & Stockton, A., 1989. *Hot spots in Extragalactic Radio Sources*, p.115, eds Meisenheimer, K. & Röser, H.-J., Springer, Berlin
Crane, P. & Stiavelli, M., 1992, MNRAS 257, 17
Dreher, J.W., 1981, AJ 86, 833
Gunn, J.E., Hoessel, J.E., Westphal, J.A., Perryman, M.A.C. & Longair, M.S., 1981, MNRAS 194, 111

Hargrave, P.J. & Ryle, M., 1974, MNRAS 166, 305
Hargrave, P.J. & Ryle, M., 1976, MNRAS 175, 481
Harris, D.E., Carilli, C.L. and Perley, R.A., 1994, Nature 367, 713
Hayes, D.S., 1985. *Calibration of Fundamental Stellar Quantities, IAU Symp. No. 111*, p.225, eds Hayes, D.S. et al., Reidel, Dordrecht
Heavens, A.F. and Meisenheimer, K. 1987, MNRAS 225, 335
Hiltner, P., Meisenheimer, K., Röser, H.-J., Laing, R.A. and Perley, R.A. 1994, A&A 286, 25
Keel, W.C., 1988, ApJ 329, 532
Kössl, D., Müller, E. and Hillebrandt, W. 1990, A&A 229, 378
Kronberg, P.P., 1976, ApJ 203, L47
Kronberg, P.P., van den Bergh, S. & Button, S., 1977, AJ 82, 315 Erratum: AJ 82 1039
Laing, R.A., 1981, MNRAS 195, 261
Le Fèvre, O. & Hammer, F., 1988, ApJ 333, L37
Lelièvre, G. & Wlérick, G., 1975, A&A 42, 293
Linfield, R., 1981, ApJ 244, 436
Longair, M.S., 1977, MNRAS 173, 309
Lonsdale, C.J., Hartley-Davies, R. & Morison, I., 1983, MNRAS 202, 1
Lonsdale, C.J. & Barthel, P.D., 1986, AJ 92, 12
Meisenheimer, K, 1996. In "Jets from stars an active galactic nuclei", W. Kundt (ed.), Springer Lecture Notes No. 471, p.57
Meisenheimer, K. & Röser, H.-J., 1986, Nature 319, 459
Meisenheimer, K. and Heavens, A.F., 1986, Nature 323, 419
Meisenheimer, K., Röser, H.-J., Hiltner, P.R., Yates, M.G., Longair, M.S., Chini, R. & Perley, R.A., 1989, A&A 219, 63
Meisenheimer, K., Röser, H.-J. and Schlötelburg, M., 1996a, A&A 307, 61
Meisenheimer, K, Neumann, M. and Röser, H.-J. 1996b. In "Jets from stars an active galactic nuclei", W. Kundt (ed.), Springer Lecture Notes No. 471, p.230.
Miley, G.K. & Wade, C.M. 1971, ApJL 8, 11
Neumann, M., Meisenheimer, K., Röser, H.-J. and Stickel, M., 1995, A&A 296, 662
Neumann, M., 1995. PhD Thesis, Heidelberg
Neumann, M., Meisenheimer, K. and Röser, H.-J., 1996, Submitted to A&A
Okayasu, R. Ishiguro, M. and Tabara, H., 1992, PASJ 44, 335
Perley, R.A., 1989. *Hot spots in Extragalactic Radio Sources*, p.1 eds Meisenheimer, K. & Röser, H.-J., Springer, Berlin
Perley, R.A., Röser, H.-J. and Meisenheimer, K., 1997, A&A in press
Pooley, G.G. & Henbest, S.N., 1974, MNRAS 169, 477
Rieke, G.H. & Lebofsky, M.J., 1985, ApJ 288, 618
Röser, H.-J., 1989. *Hot spots in Extragalactic Radio Sources*, p.91, eds. Meisenheimer, K. & Röser, H.-J., Springer, Berlin
Röser, H-J. and Meisenheimer, K., 1987, ApJ 314, 70
Röser, H.-J., Meisenheimer, K. and Perley, R. A., 1996a, In "Cygnus A: Study of a Radio Galaxy", C.L.Carilli & D.E. Harris (eds.), Cambridge University press, p. 121
Röser, H.-J., Meisenheimer, K., Perley, R. A., and Conway, R. G. 1996b In preperation.
Roland, J., Pelletier, G. and Muxlow T.W.B., 1988, A&A 207, 16
Spinrad, H. & Stauffer, J.R., 1982, MNRAS 200, 153
Swarup, G., Thompson, A. & Bracewell, R., 1963, ApJ 138, 305
Thomson, R.C., Crane, P. and MacKay, C.D., 1995, ApJL 446, L93
van den Bergh, S., 1976, ApJ 210, L63
Wright, M. & Birkinshaw, M., 1984, ApJ 281, 135
Yee, H. & Oke, J.B., 1978, ApJ 226, 753

This article was processed by the author using Springer-Verlag LaTeX A&A style file *L-AA* version 3.